Chemical Science

ROYAL SOCIETY OF CHEMISTRY

EDGE ARTICLE

View Article Online
View Journal

Cite this: DOI: 10.1039/d5sc07564e

All publication charges for this article have been paid for by the Royal Society of Chemistry

Electrolyte concentration modulates the surface structure evolution of Au(111) cathodes

Yue Feng,†[ab] Yu-Qi Wang,†*[a] Jiaju Fu,[a] Zi-Cong Wang,[ab] Dong Wang*[ab] and Li-Jun Wan*[ab]

Received 30th September 2025
Accepted 6th January 2026

DOI: 10.1039/d5sc07564e

rsc.li/chemical-science

Understanding the *in situ* surface structure of electrodes is crucial for unraveling the synergistic mechanisms of electrolytes in interfacial electrocatalysis. Herein, using *in situ* electrochemical scanning tunneling microscopy (EC-STM), we unveil the electrolyte concentration-driven roughening of Au(111) surfaces under cathodic polarization. As the concentration of alkali metal cations (AM^+) ([AM^+]) decreases, the AM^+-induced surface structure evolution proceeds from surface corrosion at 1 M to the formation of surface pits alongside surface nanoclusters composed of released Au atoms at 0.5–0.3 M and ultimately to the generation of pit-free nanoclusters *via* surface atomic migration at 0.2 M. Moreover, surface modifications modulate the electrode surface structure, enabling more pronounced structure evolution at lower bulk [AM^+]. Electrochemical measurements correlate increased surface roughness with enhanced CO_2 reduction reaction (CO_2RR) performance. The results provide a new perspective on understanding the role of AM^+ in regulating the electrochemical interface and microscopic insights into AM^+ concentration-driven *in situ* surface structures, which is important for understanding electrolyte-mediated surface structure–activity relationships.

Introduction

The nanoscale surface morphology of catalysts decisively determines the thermodynamics and kinetics of reactions.[1–3] The surface structure of metal electrodes dictates the coordination environment and thereby affects the electronic properties and catalytic performance of metal surface atoms.[4] Extensive studies have shown that the facets, nanostructures, defects, and stresses on the catalyst surface considerably affect the reaction performance including the CO_2 reduction reaction (CO_2RR), O_2 reduction reaction (ORR), H_2 evolution reaction (HER), and N_2 reduction reaction (NRR).[5–11] Recently, it was reported that the electrode surface of metals, metal oxides and carbon-based single-atom catalysts undergoes structure evolution during electrocatalysis, modulating the reaction activity and selectivity accordingly.[12–20] For instance, CO induces Cu surface restructuring and regulates the dissolution and redeposition of surface Cu atoms, which notably affects the electrocatalytic performance of Cu.[21–23] During electrochemical redox cycles, O atoms bound to the Pt(111) surface exchange positions with surface Pt atoms and roughen the Pt surface.[24,25] Uncovering the *in situ* surface morphology of electrodes under reaction conditions relies on characterization techniques with nanometer spatial resolution, such as electrochemical scanning tunneling microscopy (EC-STM),[24–29] electrochemical atomic force microscopy (EC-AFM),[30,31] and transmission electron microscopy (TEM).[15,32,33] Establishing *in situ* structure–activity relationships is fundamentally important for designing and stabilizing high-performance surface structures.

The *in situ* surface structure of electrodes is greatly affected by the electrolyte species at the interface. For instance, the dissolution of Cu^+ species from Cu electrodes upon anodic potential pulse is controlled by the type of alkali metal cation (AM^+), which modulates the metal redeposition and the surface structure.[34] Au is generally regarded as a relatively stable electrode, and its structure evolution is typically observed under anodic or intense cathodic polarization conditions.[35–38] Recently, we have shown that large AM^+ induces surface structure evolution of Au during cathodic polarization, generating highly active sites that substantially increase CO_2RR activity.[39] The *in situ* surface structure of electrodes under the influence of AM^+ is governed by modulation of the electric double layer (EDL), including hydrated ion structures, interfacial water organization, and surface adsorption.[21–23,34,39–41] As the AM^+ concentration critically shapes the EDL, its role in determining the surface structure merits detailed investigation. Additionally, the AM^+ concentration strongly affects the performance of many cathodic reactions.[42–49] Despite the growing attention on the underlying synergistic mechanism, currently, the correlation

[a]CAS Key Laboratory of Molecular Nanostructure and Nanotechnology, CAS Research/Education Center for Excellence in Molecular Sciences, Beijing National Laboratory for Molecular Science, Institute of Chemistry, Chinese Academy of Sciences, Beijing 100190, China. E-mail: wyqchem@iccas.ac.cn; wangd@iccas.ac.cn; wanlijun@iccas.ac.cn

[b]University of Chinese Academy of Sciences, Beijing 100049, China

† These authors contributed equally to this work.

between the electrolyte concentration and *in situ* surface structure of electrodes has yet to be clarified. Relevant microscopic evidence regarding these issues is highly desired yet still scarce, which limits the insight into the interfacial processes and the origin of the electrochemical activity.

Here, we demonstrate that the *in situ* surface structure evolution of Au electrodes under cathodic polarization strongly depends on the electrolyte type, concentration, and surface modifications by *in situ* EC-STM. Increased [AM^+] not only changes the restructuring of Au(111) but also shifts the critical potential for restructuring positively. Intriguingly, surface modifications with aromatic carboxylic acids on Au(111) further change the extent of surface structure evolution. Correlative morphological and electrochemical measurements establish the direct structure–activity relationship of roughened electrodes. The results provide new insights into the role of [AM^+] at the electrochemical interface and in electrochemical processes.

Methods

Chemicals

O-phthalaldehyde (OPA) was from Sigma-Aldrich (≥99%). Phthalic acid (PA) was from Sigma-Aldrich (≥99.5%). Trimesic acid (TMA) was from Sigma-Aldrich (95%). Li_2CO_3 (Sigma-Aldrich, 99.99% trace metals basis), $NaHCO_3$ (MACKLIN, 99.99% metals basis), $KHCO_3$ (Aladdin, ≥99.99% metals basis), Rb_2CO_3 (MACKLIN, 99.9% metals basis) and $CsHCO_3$ (MACKLIN, 99.99% trace metals basis) were used. $LiHCO_3$ and $RbHCO_3$ electrolytes were prepared by saturating CO_2 in Li_2CO_3 and Rb_2CO_3 electrolytes, respectively. KOH was from J&K (purity > 90%). Octahedral Au NPs were from Wuhan MiCe Technology Co., Ltd. Milli-Q water (18.2 MΩ cm, TOC < 4 ppb) was used throughout the investigation.

EC-STM measurements

All EC-STM images were collected using a NanoScope E scanning tunneling microscope (Bruker, Inc.). A tungsten wire (Alfa Aesar, 0.25 mm in diameter) was electrochemically etched (0.6 M KOH, 20 V DC) and insulated by coating to prepare the EC-STM tips. The Au(111) single crystal prepared by the Clavilier method was used as the working electrode. The Au(111) electrode was annealed in a hydrogen–oxygen flame before each experiment and transferred into an electrochemical cell with two platinum wires as the reference electrode and counter electrode.

Electrochemical CO_2RR measurement

XC-72R carbon black was dispersed in 10 mL ethanol and was sonicated for 1 h in an ice bath to ensure the formation of a well-dispersed suspension. The Au NPs re-dispersed in a mixed solution (ethanol/H_2O = 1 : 1) were added dropwise into the XC-72R carbon black suspension. The mass ratio of the catalysts and carbon black is 1 : 1. The obtained mixture was then sonicated for another 1 h to allow the Au NPs to be loaded onto the carbon supports. Then the AuNPs/C catalyst was obtained by centrifugation at 8000 rpm for 10 min, followed by washing twice with ethanol. The as-prepared catalyst was re-dispersed in ethanol by sonication to prepare catalyst ink with a gold concentration of 1 mg mL^{-1} and 20 μL of 5% Nafion solution. Finally, catalyst ink with a total volume of 0.5 mL was dropped onto both sides of the carbon paper (Toray TGP-H-060) with a working area of 0.5 cm × 0.5 cm, achieving a loading amount of 1 mg cm^{-2}. The obtained carbon paper electrode was dried under ambient conditions.

The electrocatalytic performance of the CO_2RR was evaluated in an H-type electrochemical cell separated by an ion-exchange membrane (Nafion-212, Sigma-Aldrich). The electrolytes were CO_2-saturated $CsHCO_3$ solutions, as described in the article. The electrochemical measurements were carried out in a three-electrode system at room temperature. An Ag/AgCl electrode (saturated KCl) and platinum mesh were used as reference and counter electrodes, respectively. All potentials were converted to those *versus* the reversible hydrogen electrode (RHE) using the following equation:

$$E(vs.\ \mathrm{RHE}) = E(vs.\ \mathrm{Ag/AgCl}) + 0.197\ \mathrm{V} + 0.0592 \times \mathrm{pH\ V}$$

Both sides of the H-type electrochemical cell contained 10 mL of electrolyte with 15 mL of headspace. The electrolyte was purged with CO_2 for 30 min under vigorous stirring before tests. The flow rate of CO_2 was controlled at 10 standard cubic centimeters per minute (sccm) using an electronic gas controller and then routed directly into the gas sample loop of GC. The gaseous phase composition was analyzed by GC every 15 min after the current was stable.

Results and discussion

Au(111) surface structure evolution depends on the AM^+ concentration

EC-STM is conducted to investigate the correlation between the *in situ* surface structure of Au(111) under cathodic polarization and the interfacial AM^+ species and their concentrations. Fig. 1 shows the surface structure evolution of Au(111) in 1 M CO_2-saturated $AMHCO_3$ ($AM^+ = K^+$, Rb^+, and Cs^+) electrolytes. In 1 M $CsHCO_3$ electrolyte, after the potential step from 0 V to −0.1 V *vs.* RHE, massive pits emerge on the originally flat Au(111) terrace, which indicates the extraction of Au atoms from the topmost layers. Moreover, substantial Au atoms at the terrace edge are extracted and the step becomes curved. At 100 s, the corrosion of topmost Au(111) layers increases and the release of Au atoms from deeper layers occurs (Fig. S1). The original topmost Au(111) layers have been mostly corroded by 150 s. Similar cathodic structure evolution is observed in CO_2-saturated 1 M $RbHCO_3$ and 1 M $KHCO_3$ electrolytes (Fig. 1, S2 and S3). The Au(111) surface corrosion in Rb^+ electrolyte occurs at −0.1 V. At 150 s after the potential step, the majority of the topmost layer has been corroded, which is slower than that in Cs^+ electrolyte. In K^+ electrolyte, surface corrosion occurs at −0.1 V and the rate of the corrosion drastically slows down compared with that in Cs^+ and Rb^+ electrolytes. As shown in Fig. 1, at 150 s after the potential step in K^+ electrolyte, only

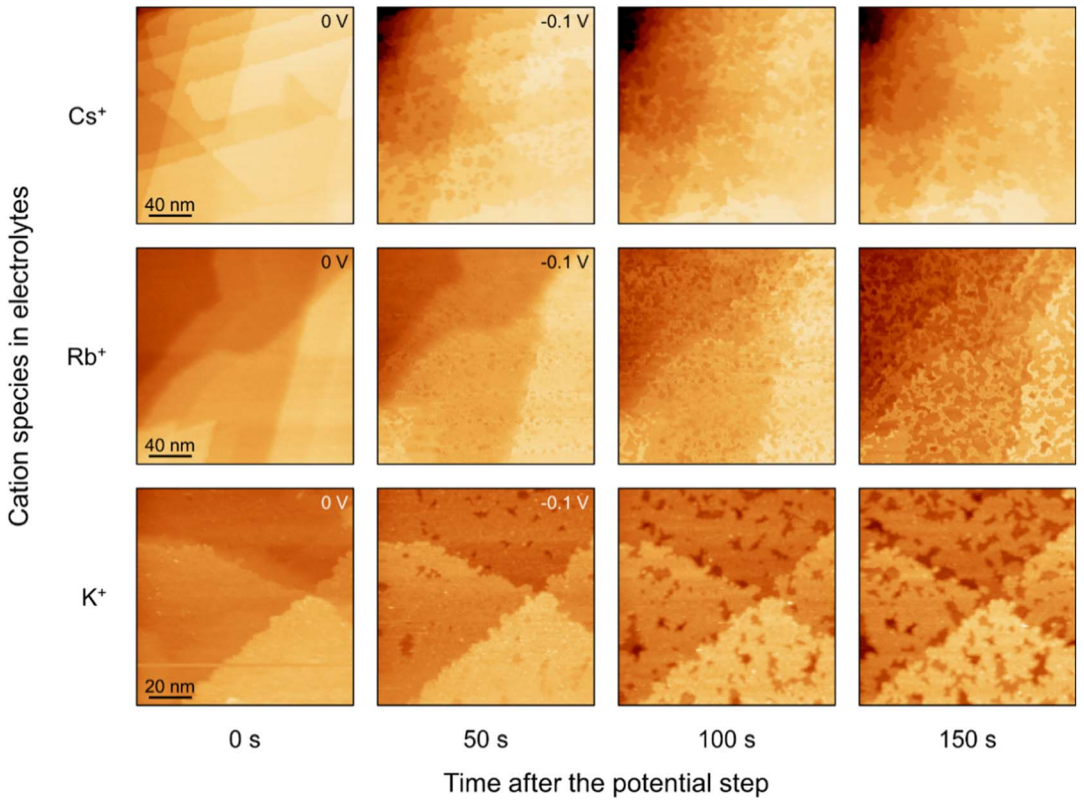

Fig. 1 EC-STM images of Au(111) in CO_2-saturated 1 M $AMHCO_3$ ($AM^+ = K^+$, Rb^+, and Cs^+) electrolytes after the potential step from 0 V to −0.1 V.

a few surface pits appear. The extent of surface corrosion is remarkably reduced in the order $Cs^+ > Rb^+ > K^+$. The surface corrosion of Au(111) is not observed at −0.1 V in 1 M CO_2-saturated $NaHCO_3$ and $LiHCO_3$ electrolytes (Fig. S4). These results demonstrate that the surface corrosion in 1 M AM^+ electrolyte strongly depends on the type of AM^+, with large cations substantially favouring the corrosion process.

To uncover the dependence of surface structure evolution on $[AM^+]$, EC-STM is performed to resolve the *in situ* surface structure of Au(111) at decreased $[AM^+]$. As shown in Fig. 2a and S5, in CO_2-saturated 0.5 M $CsHCO_3$ electrolyte, surface structure evolution occurs after the potential step from −0.1 V to −0.2 V. Adjacent surface pits and clusters are generated, showing the release of surface Au atoms and the clustering of the released atoms. Over time, the Au(111) surface becomes increasingly rough due to the continuous release, migration and aggregation of Au atoms of the top several layers (Fig. 2b and S6). At 300 s after the potential step, the originally flat Au(111) evolves into a severely roughened surface rich in pits and clusters. Cross-section analysis (Fig. 2a) suggests that the undulation of the surface roughened at −0.2 V in 0.5 M $CsHCO_3$ electrolyte is *ca.* 1.2 nm (*ca.* 5 atomic layers of Au). Furthermore, EC-STM reveals the effect of AM^+ types (Cs^+, Rb^+, and K^+) on the surface structure of Au(111) in 0.5 M electrolyte at −0.2 V (Fig. S7). It is shown that large AM^+ is more conducive to the release and clustering of surface Au atoms. In contrast to the robust corrosion at $[AM^+]$ of 1 M, the formation of Au clusters commences during the surface structure evolution in 0.5 M AM^+ electrolytes. The critical cathodic potential for Au(111) structure evolution becomes more negative in 0.5 M AM^+ electrolytes than in 1 M AM^+ electrolyte.

We further studied the Au(111) surface structure evolution in CO_2-saturated 0.4 M and 0.3 M $CsHCO_3$ electrolyte. Compared to that in 0.5 M electrolyte, lowering $[Cs^+]$ to 0.4 M decreases the quantity of pits and clusters on the Au(111) surface at −0.2 V (Fig. S8), showing reduced release and aggregation of surface Au atoms. In 0.3 M electrolyte, Au(111) reconstruction lines are clearly observed on the surface at −0.1 V (Fig. 2c and S9). After the potential step from −0.1 V to −0.2 V, pits extending in the direction parallel to reconstruction lines appear on the surface (shown by the white arrow in Fig. 2c), demonstrating the release of surface Au atoms. Moreover, Au clusters are generated around the pits, showing that the surface Au atoms released at the pits aggregate into adjacent clusters (shown by the black arrow in Fig. 2c). The process of surface structure evolution at decreased $[AM^+]$ consists of release, migration, and aggregation of surface Au atoms, leading to the formation of Au clusters and pits (Fig. S10). Additionally, the extent and rate of Au(111) surface structure evolution are positively correlated with $[AM^+]$.

When the bulk $[AM^+]$ is further decreased to 0.2 M, different morphological evolutions of Au(111) are resolved by EC-STM. As shown in Fig. 3a, an atomically flat Au(111) surface is observed at −0.2 V in CO_2-saturated 0.2 M $CsHCO_3$ electrolyte. After the applied potential is negatively shifted to −0.3 V, Au clusters appear on the Au(111) surface, and the surface density of Au clusters gradually increases with time. At 25 s after the potential

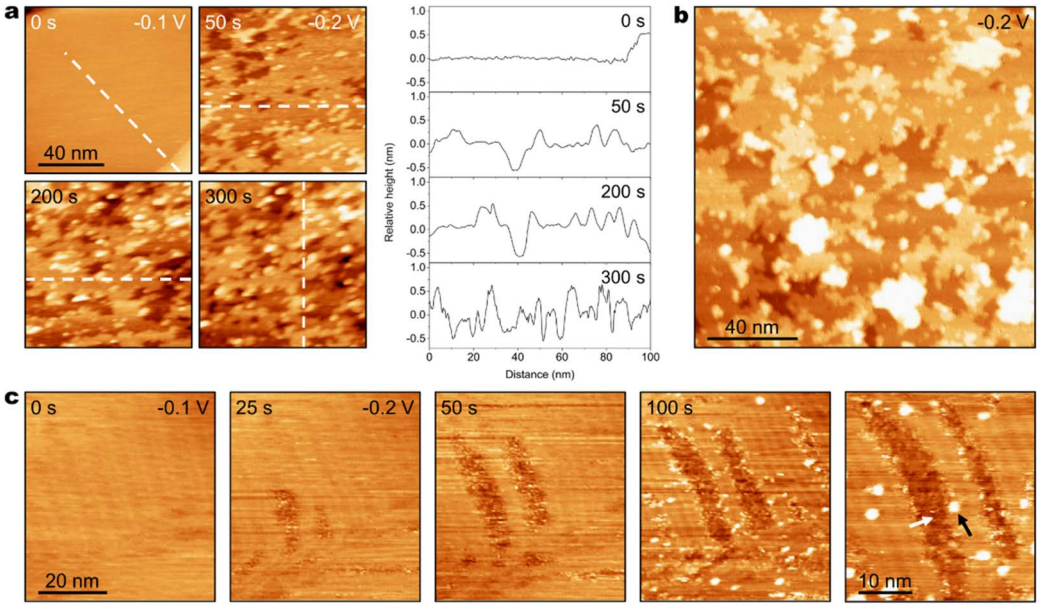

Fig. 2 (a and b) EC-STM images of Au(111) in CO_2-saturated 0.5 M $CsHCO_3$ electrolyte after the potential step from −0.1 V to −0.2 V. (a) Time-dependent surface structure after the potential step. Cross-section corresponding to the dashed line. (b) Surface structure at 150 s after the potential step. (c) EC-STM images of Au(111) in CO_2-saturated 0.3 M $CsHCO_3$ electrolyte after the potential step from −0.1 V to −0.2 V.

step, several Au clusters emerge on the surface. After 225 s, the quantity of Au clusters has increased significantly. At 250 s, the surface is covered by substantial amounts of Au clusters. At 275 s, the surface has been severely roughened. The surface density of Au clusters essentially ceases to increase after 350 s (Fig. S11). Cross-section analysis (Fig. 3b) shows surface undulation after roughening in 0.2 M $CsHCO_3$ electrolyte at −0.3 V is *ca.* 0.7 nm (*ca.* 3 atomic layers of Au). Notably, instead of surface corrosion in high [AM^+] electrolytes, prominent cluster formation occurs in 0.2 M Cs^+ electrolyte.

Furthermore, the surface coverage of the Au clusters is evaluated using the proportion of the projected area of the clusters to the scan area. Particle analysis of STM data is performed to quantitatively assess the surface proportion of the roughened area ($P_{roughened}$), which is obtained from dividing the projected area of Au clusters by the scan area (Fig. S12). The time-dependent $P_{roughened}$ on the Au(111) surface after the potential step from −0.2 V to −0.3 V in CO_2-saturated 0.2 M $CsHCO_3$ electrolyte is shown in Fig. 3c. During the *in situ* surface structure evolution, $P_{roughened}$ increases with time, which grows slowly in the early stage of structure evolution (before 125 s) when the surface coverage of Au clusters is low and rapidly in the late stage of roughening (after 125 s) when the cluster coverage becomes relatively higher. These results

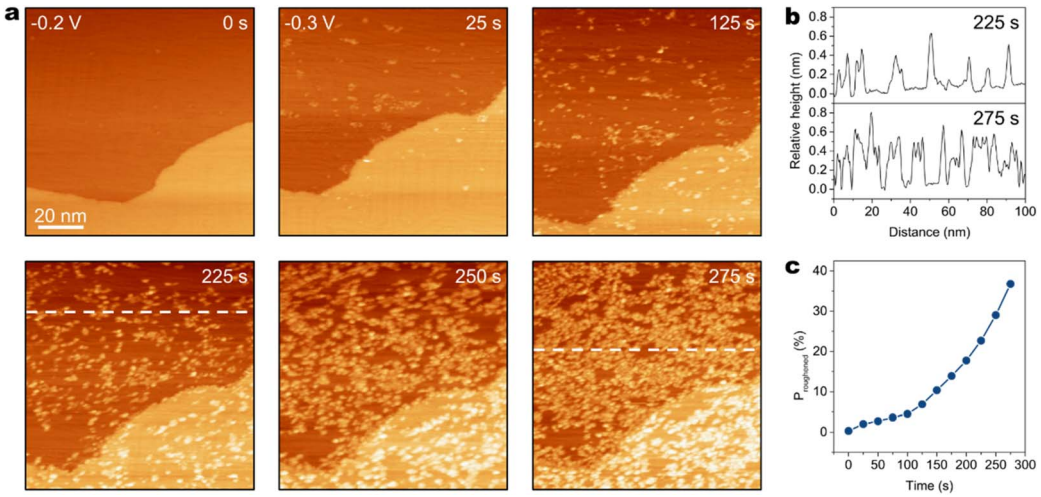

Fig. 3 (a) EC-STM images of Au(111) in CO_2-saturated 0.2 M $CsHCO_3$ electrolyte after the potential step from −0.2 V to −0.3 V. (b) Cross-section corresponding to the dashed line in (a). (c) Time dependence of $P_{roughened}$ after the potential step from −0.2 V to −0.3 V.

demonstrate the correlation between the generation rate of Au clusters and the surface coverage of Au clusters. It is reported that surface Au clusters are rich in under-coordinated Au atoms, which possess relatively high surface mobility.[28,39,50] The clusters are formed due to the migration and aggregation of surface metal adatoms.[14,21,22,39,50] Increasing the quantity of surface atoms with high mobility improves the probability of atomic aggregation on the surface. Therefore, the formation of Au clusters is favored by higher surface density of clusters.

Overall, the elevated interfacial [AM^+] leads to more severe roughening at more positive cathodic potentials. The critical potential for the cluster formation is −0.4 V in 0.1 M $CsHCO_3$ electrolyte,[39] which is advanced to −0.3 V in 0.2 M $CsHCO_3$ electrolyte with *ca.* 0.7 nm surface undulation. The slightly increased [AM^+] from 0.1 M to 0.2 M barely changes the roughened surface structure. In 0.3 M, 0.4 M and 0.5 M $CsHCO_3$ electrolyte, the surface structure evolution occurs at −0.2 V. The surface process consists of release, migration, and clustering of Au atoms. Eventually, the surface is severely roughened with an undulation of *ca.* 1.2 nm (in 0.5 M $CsHCO_3$ electrolyte). Increasing [AM^+] to 0.3–0.5 M not only leads to the more positive critical potential for roughening, but also alters the process and morphology of the surface structure evolution. When the [AM^+] is further increased to 1 M, the critical cathodic potential is advanced to −0.1 V. The structure evolution is dominated by rapid surface corrosion and the formation of Au clusters is barely observed. Moreover, the effects of CO_2 and HCO_3^- on surface structure evolution are minor compared with that of AM^+ (Fig. S13), which can be attributed to their weak interactions with Au.[39,51] In addition, X-ray photoelectron spectroscopy (XPS) reveals that the surface structure evolution at different [AM^+] does not involve impurities typically present in AM^+-based electrolytes (Fig. S14).[38,52,53]

Scheme 1 summarizes the influence of [AM^+] on the surface structure evolution of Au(111) under cathodic polarization. It has been reported that AM^+ modulates the potential profile and the local electric field within the EDL.[48,54,55] Increasing [AM^+] compresses the EDL and enhances the interfacial electric field, which may facilitate surface atom extraction,[56] thereby leading to enhanced surface restructuring and a less negative critical potential. The larger AM^+ is partially dehydrated and accumulates in the EDL,[57] which further strengthens the local electric field and is more effective in driving Au(111) surface restructuring. Nevertheless, due to the complexity of the present systems, the detailed mechanism of surface restructuring necessitates further investigation, particularly from a theoretical perspective.

Surface structure evolution of modified electrodes under cathodic polarization

Surface modification of electrodes has emerged as an effective strategy for tuning interfacial electrochemical processes.[58–60] Previous studies have demonstrated that surface modifiers increase the interfacial [AM^+].[61–63] Here, aromatic carboxylic acid-modified Au(111) is selected to investigate the role of carboxyl in the surface structure evolution of Au electrodes and corresponding interfacial electrochemical processes. First, EC-STM is employed to observe the *in situ* surface structure of the modified Au electrodes under cathodic polarization. Fig. 4a shows the adsorbed phthalic acid (PA) on Au(111) in CO_2-saturated 0.1 M $CsHCO_3$ electrolyte containing 10 mM PA. The PA molecules form the self-assembled monolayer at −0.1 V. Each PA molecule is observed as a bright spot in the EC-STM image. The Au(111) surface is exposed at the domain boundary and the periodic vacancies in the monolayer. Afterwards, the applied potential is negatively shifted to −0.2 V, and the *in situ* surface structure of electrodes is probed by EC-STM (Fig. S15). As shown in Fig. 4b, at 125 s after the potential step, the formation of surface pits occurs and Au clusters are generated around the pits. At 250 s after the potential step (Fig. 4c), the surface density of Au clusters and pits has increased with time. Cross-section analysis quantitatively shows that the extraction of Au atoms during the structure evolution at −0.2 V occurs predominantly in the topmost layers of the Au(111) surface. In the zoomed-in EC-STM image (Fig. 4d), the ordered PA monolayer (shown by the white arrow) is maintained in the unroughened region. Overall, EC-STM reveals that PA modification facilitates the surface structure evolution of Au electrodes under cathodic polarization.

Notably, PA modification results in a more positive critical potential for surface structure evolution of Au(111) in 0.1 M Cs^+ electrolyte to −0.2 V, which is close to that in electrolytes with increased [Cs^+] to 0.3–0.5 M. Moreover, the roughening morphology of the surface with PA modification in 0.1 M Cs^+

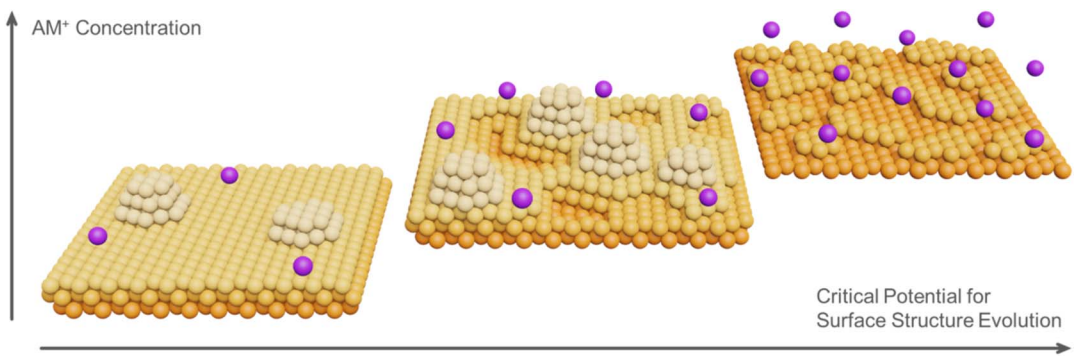

Scheme 1 Influence of [AM^+] on the surface structure evolution of Au(111) under cathodic polarization.

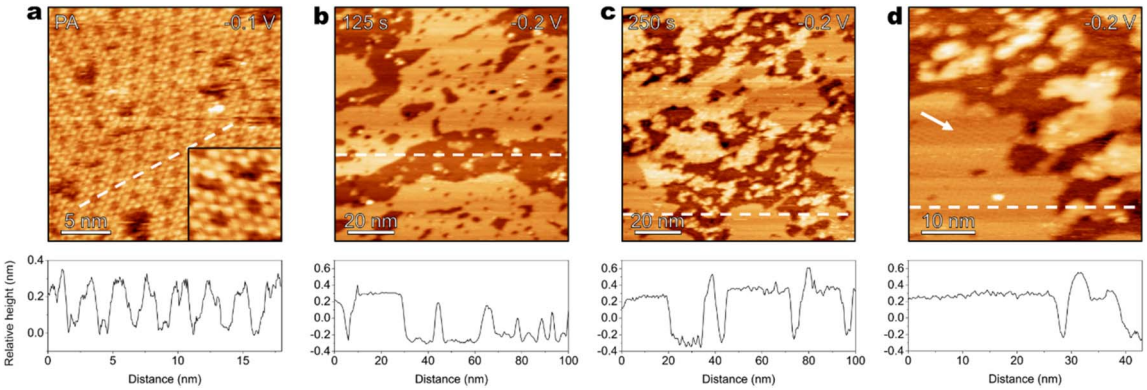

Fig. 4 (a–d) EC-STM images of Au(111) in CO_2-saturated 0.1 M $CsHCO_3$ electrolyte containing 10 mM PA at (a) −0.1 V and at (b) 125 s and (c) 250 s after the potential step from −0.1 V to −0.2 V. (d) Zoomed-in EC-STM image at −0.2 V. The cross-section corresponds to the dashed line.

electrolyte is similar to that in 0.3–0.5 M Cs^+ electrolytes. To investigate whether the promoted surface structure evolution under cathodic polarization is correlated with the type of AM^+, EC-STM is conducted to resolve Au(111) in CO_2-saturated 0.1 M $NaHCO_3$ electrolyte containing 10 mM PA (Fig. S16). Structure evolution of the PA-modified surface does not occur at −0.2 V, suggesting that the promoted structure evolution (Fig. 4) is attributed to the synergy between PA and Cs^+.

To further investigate the possibility of involvement of the carboxyl group of PA and AM^+ in affecting the surface restructuring,[64] we comparatively imaged the *in situ* surface structure of Au(111) electrodes modified with trimesic acid (TMA) and *o*-phthalaldehyde (OPA) under cathodic polarization. The self-assembled TMA monolayer forms on the Au(111) surface at −0.1 V in CO_2-saturated 0.1 M $CsHCO_3$ electrolyte containing 10 mM TMA (Fig. S17). When the applied potential is negatively shifted to −0.2 V, the surface undergoes severe roughening (Fig. S17). Massive pits commence on the electrode due to the release of surface Au atoms, and substantial clusters are generated in the vicinity of the pits, showing that the clusters are composed of the released Au atoms. Compared to PA, TMA modification leads to more pronounced surface structure evolution of electrodes, showing its stronger promoting effect on the structure evolution than PA. Moreover, EC-STM is performed to resolve the Au(111) surface in CO_2-saturated 0.1 M $CsHCO_3$ electrolyte containing 10 mM OPA. When the applied potential is negatively shifted from −0.1 V to −0.2 V, surface structure evolution barely emerges on the OPA-modified Au(111) surface, and the OPA monolayer is basically maintained (Fig. S18), demonstrating that the effect of OPA on promoting surface structure evolution of electrodes is considerably less than that of PA and TMA. These results suggest that the carboxyl group of PA and TMA can enhance the cation effect by promoting the surface Au atom pull-out and the formation of pits and Au clusters at more positive cathodic potentials, similar to that observed at relatively higher bulk $[AM^+]$.

Correlative surface structure and CO_2RR performance

The effect of surface structure evolution modulated by the electrolyte concentration and surface modification on the CO_2RR performance is explored through correlative electrochemical measurements and EC-STM. Here, octahedral Au nanoparticles (Au NPs) enclosed by Au(111) facets (Fig. S19 and S20) are employed as CO_2RR electrocatalysts. The CO partial current density and the CO faradaic efficiency (FE_{CO}) of Au NPs in 0.1 M $CsHCO_3$ electrolyte at −0.8 V are *ca.* −2.4 mA cm^{-2} and *ca.* 84%, respectively (Fig. S21). Furthermore, Au NP electrodes are pretreated under various conditions, followed by electrochemical CO_2RR measurements to disentangle the contribution of surface structure evolution to catalytic performance. First, Au NP electrodes are roughened at −0.8 V in various electrolytes for 15 min and then rinsed, followed by CO_2RR measurements (Fig. S21). After roughening in 0.5 M $CsHCO_3$ electrolyte, the CO partial current density and the FE_{CO} increase to *ca.* −3.8 mA cm^{-2} and *ca.* 92%, respectively. After roughening in 0.1 M $CsHCO_3$ electrolyte containing 10 mM PA, the CO partial current density is *ca.* −3.7 mA cm^{-2} and the FE_{CO} is *ca.* 94%. After roughening in 0.1 M $CsHCO_3$ electrolyte containing 10 mM TMA, the CO partial current density and the FE_{CO} are measured to be *ca.* −3.6 mA cm^{-2} and *ca.* 92%, respectively. Then, we evaluated the CO_2RR performance of Au NP electrodes after immersion in these electrolytes for 15 min, followed by rinsing. The CO partial current density and the FE_{CO} of the Au NP electrode after immersion in 0.5 M $CsHCO_3$ electrolyte are *ca.* −2.2 mA cm^{-2} and *ca.* 84%, respectively. After immersion in 0.1 M $CsHCO_3$ electrolyte containing 10 mM PA or TMA, the CO partial current density is *ca.* −2.3 mA cm^{-2} and −2.5 mA cm^{-2}, respectively, with the FE_{CO} measured at *ca.* 83% and 86%, respectively. These results suggest that electrochemical pretreatment in electrolytes with high $[Cs^+]$ or aromatic carboxylic acids at −0.8 V enhances the CO_2RR performance of Au NP electrodes.

To assess the impact of surface roughness on the enhanced CO_2RR performance, EC-STM is conducted to probe the surface structure of Au(111) electrodes after being held at −0.8 V for 15 min in different electrolytes (Fig. S22–S24). In CO_2-saturated 0.5 M $CsHCO_3$ electrolyte, the Au(111) surface is highly roughened at −0.8 V (Fig. S22). Cross-section analysis shows the surface undulation to be *ca.* 2 nm. In CO_2-saturated 0.1 M $CsHCO_3$ electrolyte containing 10 mM PA (Fig. S23) or 10 mM TMA (Fig. S24), both electrode surfaces undergo pronounced

roughening and become covered with a high density of Au clusters at −0.8 V, with surface undulations of *ca.* 2 nm. With reference to that observed in additive-free 0.1 M $CsHCO_3$ electrolyte reported previously,[39] increasing $[Cs^+]$ or introducing PA and TMA containing carboxyl groups significantly enhances surface roughness under CO_2RR conditions. These results demonstrate that the improved CO_2RR performance of Au NP electrodes roughened at elevated $[Cs^+]$ or in electrolytes containing PA or TMA originates from promoted surface structure evolution. The observed positive correlation between CO_2RR performance and surface roughness highlights the catalytic activity of surface clusters, aligning with previous studies that identify under-coordinated Au atoms on the clusters as highly active sites for the CO_2RR.[5,39,65] Furthermore, the results propose that increasing nanoscale surface roughness serves as a promising strategy for engineering highly active surfaces to enhance CO_2RR performance.

Conclusions

In situ STM observations reveal that the surface structure of Au(111) electrodes under cathodic polarization is intricately regulated by the type and concentration of AM^+ and surface modifications. Specifically, decreasing $[AM^+]$ shifts the critical potential for Au(111) surface structure evolution negatively. Within the $[AM^+]$ range of 0.1–1 M, higher $[AM^+]$ induces extensive surface corrosion and moderate $[AM^+]$ promotes surface Au atom pull-out leading to the formation of adjacent pits and clusters, while lower $[AM^+]$ favors the generation of surface Au nanoclusters. Additionally, elevated $[AM^+]$ accelerates the restructuring rate. These results highlight the key role of $[AM^+]$ in both the process and rate of surface structure evolution. Moreover, surface molecular modification with aromatic carboxylic acids tunes the structure evolution of Au(111), by enhancing surface roughness at low $[AM^+]$. Combining EC-STM and electrochemical measurements correlates severe surface roughening and enhanced CO_2RR performance. The *in situ* surface structure of electrodes strongly depends on electrolytes and surface modifications, which advances the fundamental understanding of interfacial electrochemistry. The results propose a new perspective that AM^+ and surface modification reshape catalysts and regulate the surface structure–activity relationship, paving the way for advanced interfacial design strategies.

Author contributions

Y. Q. W., Y. F., D. W., and L. J. W. conceived the study. Y. Q. W. and Y. F. carried out the EC-STM experiments. J. F. and Y. Q. W. conducted the electrochemical CO_2RR measurements. Y. Q. W., D. W., and L. J. W. wrote the manuscript. D. W. and L. J. W. supervised the project. All authors contributed to scientific discussions.

Conflicts of interest

The authors declare no competing interests.

Data availability

The main data supporting the findings of this study are available within the paper and its supplementary information (SI). Supplementary information: EC-STM images; XPS spectra; TEM, SEM, and UV-vis spectroscopy spectra of Au nanoparticles; electrochemical CO_2RR measurement. See DOI: https://doi.org/10.1039/d5sc07564e.

Additional data are available from the corresponding authors upon reasonable request.

Acknowledgements

This work was supported by the National Key R&D Program of China (2023YFA1500014) and the National Natural Science Foundation of China (22132007 and 22421001). The Supercomputing Environment of the Chinese Academy of Sciences is acknowledged for providing computational resources.

Notes and references

1 Y. Wang, C. Chen, X. Xiong, S. A. Skaanvik, Y. Zhang, E. D. Bøjesen, Z. Wang, W. Liu and M. Dong, *J. Am. Chem. Soc.*, 2024, **146**, 17032–17040.
2 Y. Chen, C. W. Li and M. W. Kanan, *J. Am. Chem. Soc.*, 2012, **134**, 19969–19972.
3 M. Ma, B. J. Trześniewski, J. Xie and W. A. Smith, *Angew. Chem., Int. Ed.*, 2016, **55**, 9748–9752.
4 H.-S. Su, X.-G. Zhang, J.-J. Sun, X. Jin, D.-Y. Wu, X.-B. Lian, J.-H. Zhong and B. Ren, *Angew. Chem., Int. Ed.*, 2018, **130**, 13361–13365.
5 M. Turner, V. B. Golovko, O. P. H. Vaughan, P. Abdulkin, A. Berenguer-Murcia, M. S. Tikhov, B. F. G. Johnson and R. M. Lambert, *Nature*, 2008, **454**, 981–983.
6 S. Crampton, M. D. Rötzer, C. J. Ridge, F. F. Schweinberger, U. Heiz, B. Yoon and U. Landman, *Nat. Commun.*, 2016, **7**, 10389.
7 H. Häkkinen, S. Abbet, A. Sanchez, U. Heiz and U. Landman, *Angew. Chem., Int. Ed.*, 2003, **42**, 1297–1300.
8 H.-G. Boyen, G. Kästle, F. Weigl, B. Koslowski, C. Dietrich, P. Ziemann, J. P. Spatz, S. Riethmüller, C. Hartmann, M. Möller, G. Schmid, M. G. Garnier and P. Oelhafen, *Science*, 2002, **297**, 1533–1536.
9 W. Huang, A. C. Johnston-Peck, T. Wolter, W.-C. D. Yang, L. Xu, J. Oh, B. A. Reeves, C. Zhou, M. E. Holtz, A. A. Herzing, A. M. Lindenberg, M. Mavrikakis and M. Cargnello, *Science*, 2021, **373**, 1518–1523.
10 Y. Yang, S. Louisia, S. Yu, J. Jin, I. Roh, C. Chen, M. V. F. Guzman, J. Feijóo, P.-C. Chen, H. Wang, C. J. Pollock, X. Huang, Y.-T. Shao, C. Wang, D. A. Muller, H. D. Abruña and P. Yang, *Nature*, 2023, **614**, 262–269.
11 Y. Liang, C. Csoklich, D. McLaughlin, O. Schneider and A. S. Bandarenka, *ACS Appl. Mater. Interfaces*, 2019, **11**, 12476–12480.
12 F. F. Tao, L. Nguyen, S. Zhang, Y. Li, Y. Tang, L. Zhang, A. I. Frenkel, Y. Xia and M. Salmeron, *Nano Lett.*, 2016, **16**, 5001–5009.

13 Y.-G. Kim, A. Javier, J. H. Baricuatro, D. Torelli, K. D. Cummins, C. F. Tsang, J. C. Hemminger and M. P. Soriaga, *J. Electroanal. Chem.*, 2016, **780**, 290–295.
14 L. Xu, K. G. Papanikolaou, B. A. J. Lechner, L. Je, G. A. Somorjai, M. Salmeron and M. Mavrikakis, *Science*, 2023, **380**, 70–76.
15 S. Liu, Y. Li, D. Wang, S. Xi, H. Xu, Y. Wang, X. Li, W. Zang, W. Liu, M. Su, K. Yan, A. C. Nielander, A. B. Wong, J. Lu, T. F. Jaramillo, L. Wang, P. Canepa and Q. He, *Nat. Commun.*, 2024, **15**, 5080.
16 Z. Li, L. Wang, L. Sun and W. Yang, *J. Am. Chem. Soc.*, 2024, **146**, 23901–23908.
17 M. G. Kibria, C.-T. Dinh, A. Seifitokaldani, P. D. Luna, T. Burdyny, R. Quintero-Bermudez, M. B. Ross, O. S. Bushuyev, F. P. G. de Arquer, P. Yang, D. Sinton and E. H. Sargent, *Adv. Mater.*, 2018, **30**, 1804867.
18 Y. Wang, Z. Wang, C.-T. Dinh, J. Li, A. Ozden, M. G. Kibria, A. Seifitokaldani, C.-S. Tan, C. M. Gabardo, M. Luo, H. Zhou, F. Li, Y. Lum, C. McCallum, Y. Xu, M. Liu, A. Proppe, A. Johnston, P. Todorovic, T.-T. Zhuang, D. Sinton, S. O. Kelley and E. H. Sargent, *Nat. Catal.*, 2020, **3**, 98–106.
19 K. Jiang, Y. Huang, G. Zeng, F. M. Toma, W. A. Goddard III and A. T. Bell, *ACS Energy Lett.*, 2020, **5**, 1206–1214.
20 T. J. P. Hersbach, A. T. Garcia-Esparza, S. Hanselman, O. A. P. Mellone, T. Hoogenboom, I. T. McCrum, D. Anastasiadou, J. T. Feaster, T. F. Jaramillo, J. Vinson, T. Kroll, A. C. Garcia, P. Krtil, D. Sokaras and M. T. M. Koper, *Nat. Mater.*, 2025, **24**, 574–580.
21 R. Amirbeigiarab, J. Tian, A. Herzog, C. Qiu, A. Bergmann, B. R. Cuenya and O. M. Magnussen, *Nat. Catal.*, 2023, **6**, 837–846.
22 A. Auer, M. Andersen, E.-M. Wernig, N. G. Hörmann, N. Buller, K. Reuter and J. Kunze-Liebhäuser, *Nat. Catal.*, 2020, **3**, 797–803.
23 J. Vavra, G. P. L. Ramona, F. Dattila, A. Kormányos, T. Priamushko, P. P. Albertini, A. Loiudice, S. Cherevko, N. Lopéz and R. Buonsanti, *Nat. Catal.*, 2024, **7**, 89–97.
24 L. Jacobse, Y.-F. Huang, M. T. M. Koper and M. J. Rost, *Nat. Mater.*, 2018, **17**, 277–282.
25 M. Ruge, J. Drnec, B. Rahn, F. Reikowski, D. A. Harrington, F. Carlà, R. Felici, J. Stettner and O. M. Magnussen, *J. Am. Chem. Soc.*, 2017, **139**, 4532–4539.
26 J. H. K. Pfisterer, Y. Liang, O. Schneider and A. S. Bandarenka, *Nature*, 2017, **549**, 74–77.
27 T. Kosmala, A. Baby, M. Lunardon, D. Perilli, H. Liu, C. Durante, C. Di Valentin, S. Agnoli and G. Granozzi, *Nat. Catal.*, 2021, **4**, 850–859.
28 Y. He and E. Borguet, *Faraday Discuss.*, 2002, **121**, 17–25.
29 S. Kwon, Y.-G. Kim, J. H. Baricuatro and W. A. Goddard III, *ACS Catal.*, 2021, **11**, 12068–12074.
30 G. H. Simon, C. S. Kley and B. R. Cuenya, *Angew. Chem., Int. Ed.*, 2021, **60**, 2561–2568.
31 M. Munz, J. Poon, W. Frandsen, B. R. Cuenya and C. S. Kley, *J. Am. Chem. Soc.*, 2023, **145**, 4901–5590.
32 P. L. Hansen, J. B. Wagner, S. Helveg, J. R. Rostrup-Nielsen, B. S. Clausen and H. Topsøe, *Science*, 2002, **295**, 2053–2055.
33 Q. Zhang, Z. Song, X. Sun, Y. Liu, J. Wan, S. B. Betzler, Q. Zheng, J. Shangguan, K. C. Bustillo, P. Ercius, P. Narang, Y. Huang and H. Zheng, *Nature*, 2024, **630**, 643–647.
34 Z. Li, L. Wang, L. Sun and W. Yang, *J. Am. Chem. Soc.*, 2024, **146**, 23901–23908.
35 A. I. Yanson, P. Rodriguez, N. Garcia-Araez, R. V. Mom, F. D. Tichelaar and M. T. M. Koper, *Angew. Chem., Int. Ed.*, 2011, **50**, 6346–6350.
36 T. J. P. Hersbach, I. T. McCrum, D. Anastasiadou, R. Wever, F. Calle-Vallejo and M. T. M. Koper, *ACS Appl. Mater. Interfaces*, 2018, **10**, 39363–39379.
37 M. M. Elnagar, T. Jacob and L. A. Kibler, *Electrochem. Sci. Adv.*, 2022, **2**, e2100175.
38 M. M. Elnagar, L. A. Kibler and T. Jacob, *ChemCatChem*, 2024, **16**, e202400526.
39 Y.-Q. Wang, J. Fu, Y. Feng, K. Zhao, L. Wang, J.-Y. Cai, X. Wang, T. Chen, F. Yang, J.-S. Hu, B. Xu, D. Wang and L.-J. Wan, *J. Am. Chem. Soc.*, 2024, **146**, 27713–27724.
40 Z.-M. Zhang, T. Wang, Y.-C. Cai, X.-Y. Li, J.-Y. Ye, Y. Zhou, N. Tian, Z.-Y. Zhou and S.-G. Sun, *Nat. Catal.*, 2024, **7**, 807–817.
41 H. Kim, M. M. Kim, J. Cho, S. Lee, D. H. Kim, S.-J. Shin, T. Utsunomiya, W. A. Goddard III, Y. Katayama, H. Kim and C. H. Choi, *J. Am. Chem. Soc.*, 2025, **147**, 4667–4674.
42 K. Anderson and G. Peters, *Science*, 2016, **354**, 182–183.
43 J. D. Shakun, P. U. Clark, F. He, S. A. Marcott, A. C. Mix, Z. Liu, B. Otto-Bliesner, A. Schmittner and E. Bard, *Nature*, 2012, **484**, 49–54.
44 M. Liu, Y. Pang, B. Zhang, P. D. Luna, O. Voznyy, J. Xu, X. Zheng, C. T. Dinh, F. Fan, C. Cao, F. P. G. de Arquer, T. S. Safaei, A. Mepham, A. Klinkova, E. Kumacheva, T. Filleter, D. Sinton, S. O. Kelley and E. H. Sargent, *Nature*, 2016, **537**, 382–386.
45 A. Wagner, C. D. Sahm and E. Reisner, *Nat. Catal.*, 2020, **3**, 775–786.
46 S. G. Ji, M. M. Kim, M. H. Han, J. Cho, Y. Son, Y. Y. Kim, J. Jeong, Z. H. Kim, K. H. Chae, H.-S. Oh, H. Kim and C. H. Choi, *Nat. Catal.*, 2024, **7**, 1330–1338.
47 X. Mao, X. Bai, G. Wu, Q. Qin, A. P. O'Mullane, Y. Jiao and A. Du, *J. Am. Chem. Soc.*, 2024, **146**, 18743–18752.
48 J. Resasco, L. D. Chen, E. Clark, C. Tsai, C. Hahn, T. F. Jaramillo, K. Chan and A. T. Bell, *J. Am. Chem. Soc.*, 2017, **139**, 11277–11287.
49 Z. Cui, A. J.-W. Wong, M. J. Janik and A. C. Co, *Sci. Adv.*, 2025, **11**, eadr6465.
50 Y. He and E. Borguet, *J. Phys. Chem. B*, 2001, **105**, 3981–3986.
51 J. M. Yoo, J. Ingenmey, M. Salanne and M. R. Lukatskaya, *J. Am. Chem. Soc.*, 2024, **146**, 31768–31777.
52 X. Li, C. M. Gunathunge, N. Agrawal, H. Montalvo-Castro, J. Jin, M. J. Janik and M. M. Waegele, *J. Electrochem. Soc.*, 2020, **167**, 106505.
53 A. Wuttig and Y. Surendranath, *ACS Catal.*, 2015, **5**, 4479–4484.
54 L. D. Chen, M. Urushihara, K. Chan and J. K. Nørskov, *ACS Catal.*, 2016, **6**, 7133–7139.

55 G. Hussain, L. Pérez-Martínez, J.-B. Le, M. Papasizza, G. Cabello, J. Cheng and A. Cuesta, *Electrochim. Acta*, 2019, **327**, 135055.
56 T. J. P. Hersbach and M. T. M. Koper, *Curr. Opin. Electrochem.*, 2021, **26**, 100653.
57 B. Garlyyev, S. Xue, S. Watzele, D. Scieszka and A. S. Bandarenka, *J. Phys. Chem. Lett.*, 2018, **9**, 1927–1930.
58 F. P. G. de Arquer, C.-T. Dinh, A. Ozden, J. Wicks, C. McCallum, A. R. Kirmani, D.-H. Nam, C. Gabardo, A. Seifitokaldani, X. Wang, Y. C. Li, F. Li, J. Edwards, L. J. Richter, S. J. Thorpe, D. Sinton and E. H. Sargent, *Science*, 2020, **367**, 661–666.
59 F. Li, A. Thevenon, A. Rosas-Hernández, Z. Wang, Y. Li, C. M. Gabardo, A. Ozden, C. T. Dinh, J. Li, Y. Wang, J. P. Edwards, Y. Xu, C. McCallum, L. Tao, Z.-Q. Liang, M. Luo, X. Wang, H. Li, C. P. O'Brien, C.-S. Tan, D.-H. Nam, R. Quintero-Bermudez, T.-T. Zhuang, Y. C. Li, Z. Han, R. D. Britt, D. Sinton, T. Agapie, J. C. Peters and E. H. Sargent, *Nature*, 2020, **577**, 509–513.
60 S. Banerjee, C. S. Gerke and V. S. Thoi, *Acc. Chem. Res.*, 2022, **55**, 504–515.
61 Y. Zhao, L. Hao, A. Ozden, S. Liu, R. K. Miao, P. Ou, T. Alkayyali, S. Zhang, J. Ning, Y. Liang, Y. Xu, M. Fan, Y. Chen, J. E. Huang, K. Xie, J. Zhang, C. P. O'Brien, F. Li, E. H. Sargent and D. Sinton, *Nat. Synth.*, 2023, **2**, 403–412.
62 Z. Zhu, Y. Zhu, Z. Ren, D. Liu, F. Yue, D. Sheng, P. Shao, X. Huang, X. Feng, A.-X. Yin, J. Xie and B. Wang, *J. Am. Chem. Soc.*, 2024, **146**, 1572–1579.
63 A. Wang, W. Ge, W. Sun, X. Sheng, L. Dong, W. Zhang, H. Jiang and C. Li, *Angew. Chem., Int. Ed.*, 2025, **64**, e202412754.
64 A. Sthoer, J. Hladílková, M. Lund and E. Tyrode, *Phys. Chem. Chem. Phys.*, 2019, **21**, 11329–11344.
65 S. Mezzavilla, S. Horch, I. E. L. Stephens, B. Seger and I. Chorkendorff, *Angew. Chem., Int. Ed.*, 2019, **131**, 3814–3818.